HZETRN Radiation Transport Validation Using Balloon-Based Experimental Data

James E. Warner[a,*], Ryan B. Norman[a], Steve R. Blattnig[a]

[a]*NASA Langley Research Center, Hampton, Virginia, 23681 USA*

Abstract

The deterministic radiation transport code HZETRN (High charge (Z) and Energy TRaNsport) was developed by NASA to study the effects of cosmic radiation on astronauts and instrumentation shielded by various materials. This work presents an analysis of computed differential flux from HZETRN compared with measurement data from three balloon-based experiments over a range of atmospheric depths, particle types, and energies. Model uncertainties were quantified using an interval-based validation metric that takes into account measurement uncertainty both in the flux and the energy at which it was measured. Average uncertainty metrics were computed for the entire dataset as well as subsets of the measurements (by experiment, particle type, energy, etc.) to reveal any specific trends of systematic over- or under-prediction by HZETRN. The distribution of individual model uncertainties was also investigated to study the range and dispersion of errors beyond just single scalar and interval metrics.

The differential fluxes from HZETRN were generally well-correlated with balloon-based measurements; the median relative model difference across the entire dataset was determined to be 30%. The distribution of model uncertainties, however, revealed that the range of errors was relatively broad, with approximately 30% of the uncertainties exceeding ±40%. The distribution also indicated that HZETRN systematically under-predicts the measurement dataset as a whole, with approximately 80% of the relative uncertainties having negative values. Instances of systematic bias for subsets of the data were also observed, including a significant underestimation of alpha particles and protons for energies below 2.5 GeV/u. Muons were found to be systematically over-predicted at atmospheric depths deeper than 50 g/cm^2 but under-predicted for shallower depths. Furthermore, a systematic under-prediction of alpha particles and protons was observed below the geomagnetic cutoff, suggesting that improvements to the light ion production cross sections in HZETRN should be investigated.

Keywords: Radiation Transport, Uncertainty Quantification, Model Validation

---

*Corresponding author

Email addresses: james.e.warner@nasa.gov (James E. Warner), ryan.b.norman@nasa.gov (Ryan B. Norman), steve.r.blattnig@nasa.gov (Steve R. Blattnig)

1. Introduction

With NASA's vision for space exploration emphasizing human exploration beyond the influence of Earth's geomagnetic field, radiation exposure concerns have become increasingly important. In addition to exploration, there is a growing concern for the effects of radiation on the health and safety of commercial aircrews and passengers. The concern over radiation exposure has spurred the development of radiation models including the NAIRAS model [1] for atmospheric radiation and HZETRN [2] and HETC-HEDS [3] for space radiation. As exploration moves beyond low Earth orbit (LEO) to environments where less experimental data are available, models are increasingly relied upon to make decisions regarding vehicle design and mission planning. This reliance, however, makes it critical to effectively verify and validate these models in order to determine their accuracy and reliability.

To this end, this work focuses on the validation of HZETRN, a code developed to model the transport of space radiation to determine how the radiation environment is changed by intervening materials. HZETRN solves a linearized Boltzmann equation with continuous slowing down and straight ahead approximations for computational efficiency. The code uses separate models for simulating the external radiation environment and the nuclear fragmentation of heavy ions. In this work, the 2014 Badhwar-O'Neill galactic cosmic ray (GCR) environment model [4] was used for the former, while NUCFRG3 [5] was used for the latter.

There have been several previous works aimed at validating the HZETRN code and its subcomponents. In [6], a validation study was conducted that compared two nuclear physics models (including NUCFRG3) to a database of over 3600 experimental cross sections. That work proposed new interval-based validation metrics that take into account measurement uncertainty and differentiated between model accuracy and consistency. These interval metrics were later extended in [7] to account for measurement uncertainty in both the dependent (flux) and independent (energy) variables. The study applied these metrics to validate the GCR environment models used by HZETRN against an extensive database of satellite and balloon-based measurements of differential flux.

Beyond investigating the subcomponents of the code, the work in [8] focused on validating the transport capabilities of HZETRN, comparing computed exposure quantities within shielding to measurements taken onboard the International Space Station (ISS). The study capitalized on previous efficiency improvements to HZETRN that made it feasible to generate comparisons at a statistically significant number ($\sim 77,000$) of time intervals, allowing for error estimates as a function of cutoff rigidity. Several previous works [9, 10, 11, 12] also carried out comparisons of HZETRN results with experimental data from the ISS. These studies, however, were limited by computational cost at the time and resorted to comparisons of coarser-grained, mission-averaged quantities rather than all data points along a given trajectory.

In this paper, the results of three balloon-based experiments, CAPRICE94 [13, 14], CAPRICE98 [15, 16, 17], and BESS01 [18], which measured protons, deuterons, muons, and alpha particles in the Earth's atmosphere, were compared to differential flux computed by HZETRN. The dataset consisted of 899 total measurements at energies from 0.9 GeV/u to

210.7 GeV/u and atmospheric depths of 0.0 gm/cm^2 (top of the atmosphere) to 704 g/cm^2. Model uncertainties were quantified using the interval-based validation metrics from [7] that take into account measurement uncertainty both in the flux and energy. Average uncertainty metrics were computed for the entire dataset as well as subsets of the measurements (by experiment, particle type, energy, etc.) to uncover any specific trends of systematic over- and under-prediction by HZETRN. The distribution of individual model uncertainties was also examined to study the range and dispersion of errors beyond just single scalar and interval metrics.

The remainder of the paper is organized as follows: Section 2 presents the transport algorithm employed in HZETRN and the physical approximations used to simplify the formulation and gain computational efficiency. The process of comparing differential flux computed with HZETRN against values measured from the balloon-based experiments is described in Section 3, and the validation metrics used to quantify model uncertainty are given. Finally, Section 4 and Section 5 present the results of this validation effort and summarize the findings, respectively.

2. Space Radiation Transport Formalism

HZETRN is a one-dimensional, deterministic radiation transport code which solves the Boltzmann equation within the straight ahead and continuous slowing down approximations for space radiation boundary conditions [19],

$$\left[\frac{\partial}{\partial x} - \frac{1}{A_j} \frac{\partial}{\partial E} S_j(E) + \sigma_j(E) \right] \phi_j(x, E) = \sum_k \int_E^\infty \sigma_{jk}(E, E') \phi_k(x, E') dE', \qquad (1)$$

with the boundary condition

$$\phi_j(0, E) = f_j(E), \qquad (2)$$

where A_j is the atomic mass number of a type j particle, $S_j(E)$ is the stopping power of a type j ion with kinetic energy E, $\sigma_j(E)$ is the total cross section for a type j particle with kinetic energy E, $\sigma_{jk}(E, E')$ is the inclusive production cross section for interactions where a type k particle with kinetic energy E' produces a type j particle with kinetic energy E, and $\phi_j(x, E)$ is the flux of type j particles, with energy E, at a distance x in a material. The boundary condition spectrum, $f_j(E)$ is assumed to be a known function for each particle type that is well defined over a broad energy spectrum. Note, however, that in practice the proper specification of these functions can be a significant source of uncertainty. The summation in equation (1) runs over all projectile particles that produce a type j particle.

Equation (1) is solved for cosmic ray primary particles and produced secondary particles using efficient numerical methods developed in [20] and [21] with negligible discretization error for boundary conditions, shielding materials, and shielding thickness relevant for space radiation applications. A numerical marching procedure is used with semi-analytic bi-directional solutions implemented for neutrons and light ions (Z $\leq$ 2), which allows the flux of particles at an arbitrary depth to be calculated.

3. Validation

The dataset used for validation in this study was comprised of 899 total measurements from three balloon-based experiments BESS01 [18], CAPRICE98 [15, 16, 17], and CAPRICE94 [13, 14]. These balloon-based experiments included measurements for five different particles (alphas, protons, deuterons, and positive/negative muons) at kinetic energies between 0.9 GeV/u and 210.7 GeV/u and atmospheric depths between 0.0 g/cm^2 (top of the atmosphere) and 704.0 g/cm^2. Note that the reported values for the top of the atmosphere are estimates produced through model extrapolation using the highest atmospheric measurements taken. These data were analyzed independently of the total measurement set and will be presented separately, as they serve to validate the GCR environment model used rather than the transport capabilities of HZETRN. A breakdown of measurement count across the three experiments and for the different particle types can be seen in Table 1.

The data from each balloon-based measurement included experimental uncertainty for the flux and were also grouped into energy bins. A flux-weighted mean energy was quoted for each bin in the experiments, but the actual distribution of flux in each bin was unknown. Therefore, the experimental data had both uncertainty in the flux and in the energy. The BESS01 [18] experiment separated the uncertainty in the flux into systematic and statistical components, but for our analysis these uncertainties were combined to be the square-root of the sum of the squares to be consistent with the CAPRICE98 [15, 16, 17] and CAPRICE94 [13, 14] data.

To quantify the uncertainty of HZETRN using the balloon-based data, the validation metric used needed to incorporate not only the experimental uncertainty in the flux, but also the energy binning of the data. With this in mind, the interval-based approach from [7] was adopted in this work. To facilitate a brief explanation of this metric, a graphical representation of a typical flux measurement is shown in Figure 1. Here, for a measurement taken over the energy bin $(E_0 - \Delta E^-, E_0 + \Delta E^+)$, the nominal experimental flux M_0 can be expected to fall within the interval $(M_0 - \epsilon^-, M_0 + \epsilon^+)$.

The corresponding average model flux over this same interval can be calculated as

$$\hat{F} = \frac{\int_{-\Delta E^-}^{\Delta E^+} F(E_0 + E')dE'}{\Delta E^+ + \Delta E^-}$$

$$\approx \frac{1}{N} \sum_{E_i \in [E_0 \pm \Delta E^\pm]} F(E_i), \quad (3)$$

where F is the computed flux, E_i is the ith point in the discretized energy grid used by HZETRN, and N is the number of such grid points in the particular energy bin. The relative difference between the model flux and nominal measurement value is defined as

$$R_D \equiv \frac{\hat{F} - M_0}{M_0}. \quad (4)$$

While Equation (4) is commonly used for model validation, it ignores the experimental uncertainty in the data by comparing directly with the nominal value rather than considering the range of possible measurement values.

For a more rigorous approach, the following interval-based metric was proposed in [7]

$$U_l = \frac{\hat{F} - [M_0 + \epsilon^+]}{M_0 + \epsilon^+}, \tag{5}$$

$$U_u = \frac{\hat{F} - [M_0 - \epsilon^-]}{M_0 - \epsilon^-}, \tag{6}$$

where ϵ^- and ϵ^+ are non-negative. Here, U_l and U_u define the lower and upper end of a model uncertainty interval, respectively, by comparing to the average computed flux with the bottom and top of the error bars in Figure 1. Independent of the model, the measurement uncertainty U_{exp} can also be calculated as

$$U_{\text{exp}} = \frac{\epsilon^- + \epsilon^+}{M_0}. \tag{7}$$

Equations (4) - (6) are evaluated for each available measurement and can be averaged for the entire set or subsets of the data to report a single value or interval describing the model uncertainty. Additionally, if enough data are present, the distribution of uncertainties can be determined.

4. Results

To model the balloon-based experiments, the external radiation environment was generated for the duration of each balloon flight using the 2014 version of the Badhwar-O'Neill GCR model [4]. A sharp geomagnetic cutoff, taken from the published values for each experiment (4.20 GeV/u for BESS01, 0.69 GeV/u for CAPRICE94, and 4.30 GeV/u for CAPRICE98) was then applied to the initial radiation environment, which was then transported by HZETRN through the Earth's atmosphere, modeled as 75.4% N_2, 23.3% O_2 and 1.3% Ar by mass [22].

Python scripts were developed to automate the model validation study. For each balloon-based experiment, the measurement data were first processed to generate an energy grid for HZETRN that contained a sufficient number of points within every energy bin ($E_0 - \Delta E^-, E_0 + \Delta E^+$) for the calculation of average flux in Equation (3). This energy grid and the appropriate inputs (GCR boundary conditions, geomagnetic cutoff, etc.) were used to execute HZETRN and compute average fluxes at each atmospheric depth where measurements were recorded for the balloon-based experiment being analyzed. The metrics in Equations (4) - (7) were then calculated and stored for each measurement.

First, a comparison of the measured flux data and the corresponding predicted flux with HZETRN is provided in Figure 2 for select representative cases. Here, the flux at different atmospheric depths are shown for (a) alphas from the BESS01 experiment, (b) protons from the BESS01 experiment, (c) negative muons from the CAPRICE98 experiment, and (d)

positive muons from the CAPRICE experiment. The measurement data are plotted with errors bars denoting the uncertainty in the measured flux as well as kinetic energy (from energy binning). Generally speaking, the computed values using HZETRN are well correlated with the measured flux data. A complete comparison of the balloon-based flux measurements with HZETRN predicted flux for each experiment, particle type, and atmospheric depth can be seen in the supplementary material accompanying this paper.

To quantitatively assess the agreement between model and experiment, the computed validation metrics (Eq. (4) - (7)) for the dataset (excluding top of the atmosphere data) are now examined in detail. The average model relative difference and uncertainty interval across the entire set are $\bar{R}_d = -18\%$ and $[\bar{U}_l, \ \bar{U}_u] = [-29\%, 0\%]$, respectively, indicating that there is an overall systematic under-prediction of the measurement data. Independent of the effects of cancellation, the median and mean absolute model difference for the dataset are 30% and 35%, respectively, better reflecting the true agreement between the model and the nominal experimental values. The average experimental uncertainty, $\bar{U}_{\exp} = 28\%$, is approximately equal to the width of the average uncertainty interval.

The cumulative distribution functions (CDFs) for R_d, U_l, and U_u are shown in Figure 3, illustrating the range of the uncertainties across the entire dataset. It can be seen that although the average relative difference is small, the distribution of individual errors is very broad. For example, roughly 30% of all model uncertainties are seen to exceed $\pm40\%$, with approximately 25% of those uncertainties falling below -40% and 5% above $+40\%$. This could alternatively be stated as the model uncertainties are within $\pm40\%$ at an approximate 70% confidence level [7]. A 70% confidence level is very close to one standard deviation on a normal distribution, so these are close to 1σ errors. Figure 3 also further illustrates the under-prediction of the measurement data by HZETRN as the distribution functions are shifted to the left of the y-axis, with approximately 80% of the relative uncertainties taking negative values. Note that the validation metrics in Equations (4) - (6) are bounded below by -1 but unbounded above, explaining the longer tail in the positive direction.

The average relative model uncertainties are separated by individual balloon-based experiment and shown in Table 2. It is observed that HZETRN systematically under-predicts the BESS01 measurements to a large degree while slightly over-predicting measurements from CAPRICE98. The model uncertainties are smallest in relation to the CAPRICE94 experimental data, but since they comprise less than 10% of the dataset (Table 1), this has a relatively small impact on the overall averages reported previously.

Figure 4 shows the cumulative distribution of uncertainties for the a) BESS01, b) CAPRICE94, and c) CAPRICE98 experiments. Here, the systematic under-prediction by the model of the BESS01 data and over-prediction by the model of the CAPRICE98 data is further illustrated by the shifting of the CDF to the left and right of zero on the horizontal axis, respectively. The width of the uncertainty intervals for the CAPRICE98 is larger on average as compared to the other experiments, as reflected in the average uncertainty intervals and experimental uncertainties displayed in Table 2.

The results for relative uncertainties across the individual experiments in Table 2 also highlight an interesting characteristic of the interval metrics used. It was reported in [7]

6

that the width of the uncertainty interval $[U_u, U_l]$ can be approximately interpreted as the measurement uncertainty U_{exp}. To this end, observe that

$$U_u - U_l = \hat{F} \frac{\epsilon^+ + \epsilon^-}{(M_0 + \epsilon^+)(M_0 - \epsilon^-)} \approx \hat{F} \frac{\epsilon^+ + \epsilon^-}{M_0^2}, \tag{8}$$

where it can be seen that the approximation becomes less accurate as the experimental error increases. From Equations (7) and (8), it is clear that $U_u - U_l \approx U_{\text{exp}}$ as long as $\hat{F} \approx M_0$. However, when $M_0 < \hat{F}$, the uncertainty intervals are wider than the reported experimental uncertainty and vice versa. This reasoning explains the discrepancy observed in Table 2 between the width of $\bar{U}_u, \bar{U}_l$ and $\bar{U}_{\text{exp}}$ for the three experiments. Here, the uncertainty intervals are seen to be significantly wider than the experimental uncertainty for the over-predicted experiment (CAPRICE98) and significantly narrower for the under-predicted experiment (BESS01). The attribute of the interval-based relative metric not exactly corresponding with the width of the experimental uncertainty in some cases does not change any of the analysis or conclusions in this paper. The interval-based relative metric is meant to treat the experimental values as an interval relative to the extrema of the interval, not relative to the midpoint like U_{exp}. This is the fundamental source of the difference between $U_u - U_l$ and U_{exp}. If absolute differences were considered for the metric, then there would be exact correspondence between the two.

The relative model uncertainties for each particle type are displayed in Table 3, showing the values of the metrics averaged over all experiments and measurement energies and depths for each particle. The results indicate that the overall systematic under-prediction by the model is consistent across all particle types, most significantly for alpha particles, protons, and deuterons. It can also be seen that the average experimental uncertainty, U_{exp}, is substantially less for protons and deuterons, resulting in smaller uncertainty intervals. Here, it is important to bear in mind the frequency of measurements for each particle type from Table 1. On one end, the sample size for deuteron measurements is only five, so the metrics reported in Table 3 are affected by the limited available experimental data. On the other hand, since muons account for two-thirds of the measurements, it can be expected that other aggregate metrics reported would be highly correlated with the average values of the positive and negative muons results.

Next, the average relative model difference and uncertainty intervals for different energy ranges are shown in Table 4 for protons and alphas and Table 5 for positive and negative muons. The measurement data count for each energy bin and particle type is included for illustration. The under-prediction by HZETRN noted previously in Table 3 for alpha particles and protons is seen to arise mainly from lower energy measurements (below 2.5 GeV/u) where both the magnitude of the under-prediction and measurement counts are highest. The model actually over-predicts the higher energy measurements for these particle types, albeit for a substantially smaller portion of the total dataset. Note, for muon model uncertainties in Table 5, more data were available for higher energies, with no measurements occurring below 2.5 GeV/u. The model uncertainties for muons follow a similar trend to those of the alpha particles and protons, with an under-prediction in general but an over-

prediction of positive muons and little observed bias in negative muon flux estimates for energies > 25.0 GeV/u.

The average model uncertainties below, at, and above the geomagnetic cutoff were also calculated for each light ion and are displayed for the different measurement depths in Table 6 and Table 7 for the BESS01 the CAPRICE98 experiments, respectively. Since most model flux calculated by HZETRN below the cutoff energy is due to secondary particle production, partitioning the uncertainties in this way allows for a test of the light ion production models used in the code. A small number of particles below the geomagnetic cutoff in the model results are from primary particles that have slowed to energies below the cutoff. Measurements at the top of the atmosphere were omitted since these uncertainties are due to the Badhwar-O'Neill GCR model and not the result of light ion production. Generally speaking, a systematic under-prediction of the light ions can be observed below the geomagnetic cutoff and the relative uncertainties are typically larger compared to those above the cutoff. It can also be seen that HZETRN tends to systematically over-predict light ions at energies above the cutoff, more so in Table 7 for the CAPRICE98 experiment than Table 6 for BESS01. While some of the model discrepancy for low energy light ions is due to light ion 3D effects not captured by HZETRN, it also suggests that improvements to the light ion production cross sections in the model should be investigated.

Finally, the average model uncertainties were calculated at each available measurement depth in the atmosphere and are displayed in Figure 5, where model uncertainties for alpha particles and protons at all depths are shown in (a), while uncertainties for muons are partitioned into smaller depths in (b), and larger depths in (c), for clarity. A more detailed view of this same data can be seen in Tables 8 - 10, while Table 11 displays the uncertainty metrics for top of the atmosphere measurements. Some general trends in the model uncertainties are observed from these results. First, it can be seen in Figure 5(a) that the systematic under-prediction of alpha particles and protons is consistent across the measurement depths considered. For muons, Figures 5(b) and 5(c) show that both the positive and negative muon uncertainties tend to follow similar trends across the measurement depths. It can be observed, however, that systematic under-predictions are made by HZETRN for measurements at smaller depths while over-predictions are made for larger depths. This is consistent with the straight-ahead approximation used in the transport formalism for pions and muons in HZETRN. The turning point for this trend appears to be at the measured depth of 48.4 g/cm^2, seen in more detail in Table 10.

The relative uncertainties observed for a depth of 0.0 g/cm^2 (top of the atmosphere) in Table 11 are a reflection of errors in the Badhwar-O'Neill GCR model. While it can be seen that the model predictions for protons are relatively unbiased, there is a systematic over-prediction of alpha particles in the CAPRICE94 experiment and under-prediction of alpha particles in the CAPRICE98 experiment. Since errors in these GCR boundary conditions will tend to propagate into the rest of the HZETRN results, an evaluation of available GCR models will be worthwhile to reduce uncertainties in the future.

5. Conclusion

This work presented a comparison of the high charge and energy deterministic transport code, HZETRN, against an experimental dataset of balloon-based differential flux measurements. The dataset consisted of 899 measurements total and was collected from three different experiments that included five particles (alphas, protons, deuterons, and positive/negative muons) measured at energies from 0.9 GeV/u to 210.7 GeV/u and atmospheric depths of 0.0 gm/cm^2 (top of the atmosphere) to 704 g/cm^2. Interval-based validation metrics that take into account measurement uncertainty both in the flux and the energy at which it was measured were applied to assess the HZETRN model uncertainty. Average uncertainty metrics were computed for the entire dataset as well as subsets of the measurements (by experiment, particle type, energy, etc.) to expose any specific trends of systematic over- and under-prediction by HZETRN. The distribution of individual model uncertainties was also investigated to study the range and dispersion of errors beyond just single scalar and interval metrics.

The differential fluxes from HZETRN were generally well-correlated with balloon-based measurements; the median relative model difference across the entire dataset was reported to be 30%. The distribution of model uncertainties, however, revealed that the range of errors was relatively extensive, with approximately 30% of the uncertainties found to exceed ±40%. The distribution also indicated that HZETRN systematically under-predicts the measurement dataset as a whole, with approximately 80% of the relative uncertainties taking negative values. Instances of systematic bias for subsets of the data were also observed, including a significant underestimation of alpha particles and protons for energies below 2.5 GeV/u. Muons were found to be systematically over-predicted at atmospheric depths greater than 50 g/cm^2, but under-predicted for shallower depths. Furthermore, a systematic under-prediction of alpha particles and protons was observed below the geomagnetic cutoff suggesting that improvements to the light ion production cross sections in HZETRN should be investigated.

6. Acknowledgments

[1] C. J. Mertens et al. Influence of space weather on aircraft ionizing radiation exposure. In *46th AIAA Aerospace Sciences Meeting and Exhibit*, Reno, Nevada, January 2008.

[2] J. W. Wilson, R. K. Tripathi, F. F. Badavi, and F. A. Cucinotta. Standardized radiation shield design methods: 2005 HZETRN. In *36th Conference on Environmental Systems (ICES)*, Norfolk, Virginia, 2006.

[3] L. W. Townsend, T. M. Miller, and T. A. Gabriel. HETC radiation transport code development for cosmic ray shielding applications in space. *Radiat. Prot. Dosim.*, 116:135–139, 2005.

[4] P. M. O'Neill, S. Golge, and T. C. Slaba. Badhwar - O'Neill 2014 galactic cosmic ray flux model description. NASA TP-2015-218569, 2015.

[5] A. M. Adamczyk et al. NUCFRG3: Light ion improvements to the nuclear fragmentation model. *Nucl. Instrum. Meth.*, A678(0):21–32, 2012.

[6] R. B. Norman and S. R. Blattnig. Validation of nuclear models used in space radiation shielding applications. *J. Comput. Phys*, 233:464–479, 2013.

[7] T. C Slaba, X. Xu, S. R. Blattnig, and R. B. Norman. GCR environmental models III: GCR model validation and propagated uncertainties in effective dose. *Space Weather*, 12(4):233–245, April 2014.

[8] T. C Slaba et al. Statistical validation of HZETRN as a function of vertical cutoff rigidity using ISS measurements. *Adv. Space Res.*, 47:600–610, 2011.

[9] J. W. Wilson et al. Verification and validation: High charge and energy (HZE) transport codes and future development. NASA TP-213784, 2005.

[10] J. W. Wilson et al. Time serial analysis of the induced LEO environment with the ISS 6A. *Adv. Space Res.*, 40:1562–1570, 2007.

[11] J. E. Nealy et al. Pre-engineering spaceflight validation of environmental models and the 2005 HZETRN simulation code. *Adv. Space Res.*, 40:1593–1610, 2007.

[12] M. Durante and F. A. Cucinotta. Physical basis of radiation protection in space travel. *Rev. Mod. Phys.*, 83:1245–1281, 2011.

[13] M. Boezio et al. The cosmic-ray proton and helium spectra between 0.4 and 200 GV. *Astrophys. J.*, 518(1):457–472, 1999.

[14] M. Circella et al. Measurements of primary cosmic-ray hydrogen and helium by the WiZard collaboration. *Adv. Space Res.*, 27(4):755–760, 2001.

[15] E. Mochiutti. *Atmospheric and Intersteller Cosmic Rays Measured with the CAPRICE98 Experiment.* PhD thesis, Royal Institute of Technology, 2003.

[16] E. Mocchiutti et al. Composition of cosmic ray particles in the atmosphere as measured by the CAPRICE98 balloon borne apparatus. In *28th International Cosmic Ray Conference*, Tsukuba, Japan, July 31 - August 7, 2003.

[17] M. Boezio et al. The cosmic-ray proton and helium spectra measured with the CAPRICE98 balloon experiment. *Astropart. Phys.*, 19(5):583–604, 2003.

[18] K. Abe et al. Measurements of proton, helium and muon spectra at small atmospheric depths with the BESS spectrometer. *Phys. Lett.*, B564(1-2):8–20, 2003.

[19] J. W. Wilson et al. Transport Methods and Interactions for Space Radiations. NASA RP-1257, 1991.

[20] T. C. Slaba et al. Coupled neutron transport for HZETRN. *Radiation Measurements*, 45(2):173–182, 2010.

[21] T. C. Slaba, S. R. Blattnig, and F. F. Badavi. Faster and more accurate transport procedures for HZETRN. *J. Comput. Phys.*, 229(24):9397–9417, 2010.

[22] G. De Angelis, J. M. Clem, P. E. Goldhagen, and J. W. Wilson. A new dynamical atmospheric ionizing radiation (AIR) model for epidemiological studies. *Adv. Space Res.*, 32(1):17–26, 2003.

Table 1: Measurement counts by experiment and particle type.

Experiment	Alpha	Proton	Deuteron	μ^+	μ^-	Total
BESS01	58	60	0	132	240	490
CAPRICE94	25	18	0	18	27	88
CAPRICE98	55	69	5	89	103	321
Total:	138	147	5	239	370	899

Table 2: Average relative model uncertainties for the individual balloon-based experiments.

Experiment	$\bar{R}_D$	$[\bar{U}_l, \bar{U}_u]$	$\bar{U}_{\mathrm{exp}}$
BESS01	-34%	[-42%, -23%]	29%
CAPRICE94	-3%	[-17%, 22%]	29%
CAPRICE98	7%	[-9%, 35%]	33%

Table 3: Average relative model uncertainties for individual particles.

Particle	$\bar{R}_D$	$[\bar{U}_l, \bar{U}_u]$	U_{exp}
Alpha	-28%	[-34%, -15%]	33%
Proton	-33%	[-37%, -29%]	12%
Deuteron	-47%	[-51%, -42%]	15%
μ^+	-20%	[-31%, -3%]	30%
μ^-	-10%	[-24%, 14%]	35%

Table 4: Relative model uncertainties for alpha and proton particles averaged across all experiments/depths and grouped by energy values.

Energy	Alpha			Proton		
(GeV/u)	$\bar{R}_D$	$[\bar{U}_l, \bar{U}_u]$	Count	$\bar{R}_D$	$[\bar{U}_l, \bar{U}_u]$	Count
< 2.5	-53%	[-56%, -50%]	48	-55%	[-59%, -51%]	55
2.5 - 5.0	-5%	[-11%, 1%]	19	-30%	[-33%, -27%]	23
5.0 - 10.0	-3%	[-12%, 45%]	18	-7%	[-9%, -4%]	23
10.0 - 25.0	16%	[5%, 31%]	4	17%	[10%, 27%]	5
> 25.0	19%	[10%, 31%]	2	29%	[18%, 46%]	4

Table 5: Relative model uncertainties for muon particles averaged across all experiments/depths and grouped by energy values.

Energy	Positive Muon			Negative Muon		
(GeV/u)	$\bar{R}_D$	$[\bar{U}_l, \bar{U}_u]$	Count	$\bar{R}_D$	$[\bar{U}_l, \bar{U}_u]$	Count
< 2.5	-	-	0	-	-	0
2.5 - 5.0	-17%	[-30%, 1%]	51	-18%	[-31%, 0%]	50
5.0 - 10.0	-28%	[-37%, -17%]	76	-16%	[-28%, 0%]	77
10.0 - 25.0	-28%	[-37%, -15%]	89	-14%	[-26%, 8%]	118
> 25.0	37%	[12%, 78%]	23	2%	[-17%, 34%]	125

Table 6: Relative model uncertainties below, at (±0.5GeV), and above the cutoff energy (4.2 GeV/u) for alpha, proton, and deuteron particles from the BESS01 experiment.

Particle/Depth	Below cut-off		At cut-off (±0.5GeV)		Above cut-off	
	$\bar{R}_D$	$[\bar{U}_l, \bar{U}_u]$	$\bar{R}_D$	$[\bar{U}_l, \bar{U}_u]$	$\bar{R}_D$	$[\bar{U}_l, \bar{U}_u]$
Alphas/4.58 g/cm^2	-46%	[-49%, -42%]	-23%	[-27%, -17%]	-4%	[-8%, 1%]
Alphas/10.4 g/cm^2	-55%	[-58%, -52%]	-18%	[-24%, -12%]	-12%	[-17%, -8%]
Alphas/26.4 g/cm^2	-52%	[-57%, -47%]	-16%	[-25%, -6%]	-8%	[-22%, 143%]
Protons/4.58 g/cm^2	-58%	[-60%, -55%]	-16%	[-17%, -14%]	-14%	[-16%, -13%]
Protons/10.4 g/cm^2	-54%	[-56%, -52%]	-14%	[-16%, -13%]	-13%	[-15%, -12%]
Protons/26.4 g/cm^2	-43%	[-46%, -41%]	-6%	[-8%, -4%]	-13%	[-15%, -11%]

Table 7: Relative model uncertainties below, at (±0.5GeV), and above the cutoff rigidity (4.3 GeV/u) for alpha, proton, and deuteron particles from the CAPRICE98 experiment.

Particle/Depth	Below cut-off		At cut-off (±0.5GeV)		Above cut-off	
	$\bar{R}_D$	$[\bar{U}_l, \bar{U}_u]$	$\bar{R}_D$	$[\bar{U}_l, \bar{U}_u]$	$\bar{R}_D$	$[\bar{U}_l, \bar{U}_u]$
Alphas/5.5 g/cm^2	-22%	[-24%, -20%]	15%	[11%, 19%]	22%	[12%, 35%]
Alphas/16.0 g/cm^2	-40%	[-46%, -33%]	37%	[26%, 50%]	12%	[-3%, 32%]
Protons/5.5 g/cm^2	-58%	[-60%, -55%]	9%	[8%, 12%]	10%	[8%, 13%]
Protons/23.0 g/cm^2	-53%	[-59%, -45%]	2%	[-6%, 12%]	23%	[6%, 49%]
Deuterons/5.5 g/cm^2	-47%	[-51%, -42%]	-	-	-	-

Table 8: Relative model uncertainties for alpha and proton particles averaged across all experiments/energies and grouped by depth value.

Depth	Alpha		Proton	
(g/cm^2)	$\bar{R}_D$	$[\bar{U}_l,\ \bar{U}_u]$	$\bar{R}_D$	$[\bar{U}_l,\ \bar{U}_u]$
4.58	-33%	[-36%, -29%]	-45%	[-47%, -42%]
5.5	-7%	[-11%, -1%]	-22%	[-24%, -19%]
10.4	-43%	[-46%, -39%]	-42%	[-44%, -40%]
16.0	-19%	[-28%, -8%]	-	-
23.0	-	-	-30%	[-38%, -17%]
26.4	-40%	[-47%, 3%]	-34%	[-36%, -31%]

Table 9: Relative model uncertainties for muon particles averaged across all experiments/energies and grouped by depth value (for $0 \text{ g/cm}^2 \leq \text{depth} < 20 \text{ g/cm}^2$).

Depth	Positive Muon		Negative Muon	
(g/cm^2)	$\bar{R}_D$	$[\bar{U}_l, \bar{U}_u]$	$\bar{R}_D$	$[\bar{U}_l, \bar{U}_u]$
3.9	-50%	[-53%, -45%]	-26%	[-32%, -18%]
4.58	-44%	[-54%, -30%]	-37%	[-50%, -17%]
5.45	-7%	[-17%, 7%]	15%	[3%, 30%]
5.5	-6%	[-16%, 8%]	16%	[4%, 31%]
5.99	-46%	[-53%, -36%]	-33%	[-46%, -13%]
7.85	-41%	[-48%, -32%]	-31%	[-40%, -20%]
8.79	-46%	[-51%, -40%]	-35%	[-43%, -25%]
9.45	-42%	[-49%, -34%]	-30%	[-41%, -16%]
10.4	-43%	[-49%, -35%]	-27%	[-38%, -13%]
11.9	-42%	[-48%, -35%]	-18%	[-30%, -2%]
13.4	-40%	[-46%, -33%]	-28%	[-38%, -15%]
15.0	-49%	[-59%, -34%]	-25%	[-41%, 4%]
15.5	-36%	[-43%, -29%]	-28%	[-36%, -17%]
17.5	-33%	[-39%, -27%]	-23%	[-32%, -13%]

Table 10: Relative model uncertainties for muon particles averaged across all experiments/energies and grouped by depth value (for 20 g/cm^2 ≤ depth).

Depth	Positive Muon		Negative Muon	
(g/cm^2)	$\bar{R}_D$	$[\bar{U}_l,\ \bar{U}_u]$	$\bar{R}_D$	$[\bar{U}_l,\ \bar{U}_u]$
22.6	-23%	[-38%, 0%]	13%	[-12%, 57%]
23.4	-35%	[-42%, -27%]	-19%	[-30%, -4%]
25.5	-10%	[-24%, 11%]	28%	[2%, 82%]
26.4	-33%	[-40%, -24%]	-24%	[-34%, -12%]
33.0	-37%	[-47%, -23%]	-35%	[-46%, -18%]
48.4	-12%	[-25%, 9%]	-9%	[-24%, 15%]
50.5	5%	[-9%, 25%]	21%	[3%, 50%]
77.0	2%	[-17%, 34%]	7%	[-12%, 37%]
104.0	20%	[-1%, 55%]	35%	[0%, 175%]
136.0	35%	[7%, 89%]	47%	[16%, 109%]
165.0	2%	[-13%, 23%]	40%	[14%, 85%]
219.0	7%	[-11%, 34%]	34%	[9%, 77%]
308.0	20%	[3%, 44%]	39%	[17%, 74%]
462.0	46%	[25%, 77%]	54%	[30%, 90%]
704.0	82%	[51%, 131%]	121%	[80%, 187%]

Table 11: Average relative model uncertainties for top of the atmosphere measurements.

Experiment/Particle	$\bar{R}_D$	$[\bar{U}_l, \bar{U}_u]$
CAPRICE94/Alpha	14%	[7%, 22%]
CAPRICE94/Proton	3%	[2%, 5%]
CAPRICE98/Alpha	-7%	[-11%, -3%]
CAPRICE98/Proton	1%	[-2%, 3%]
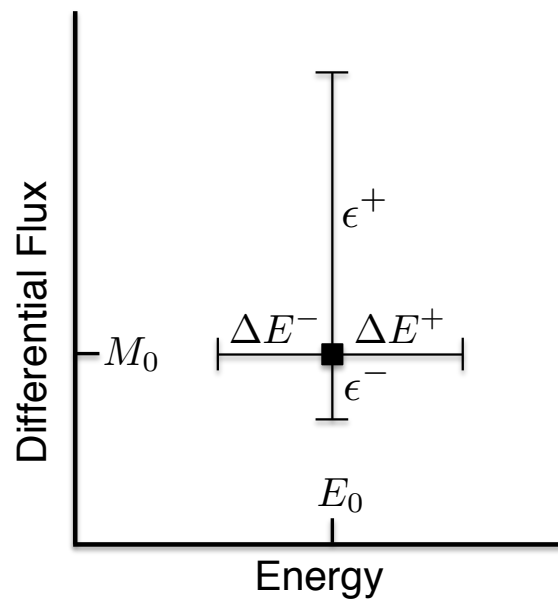
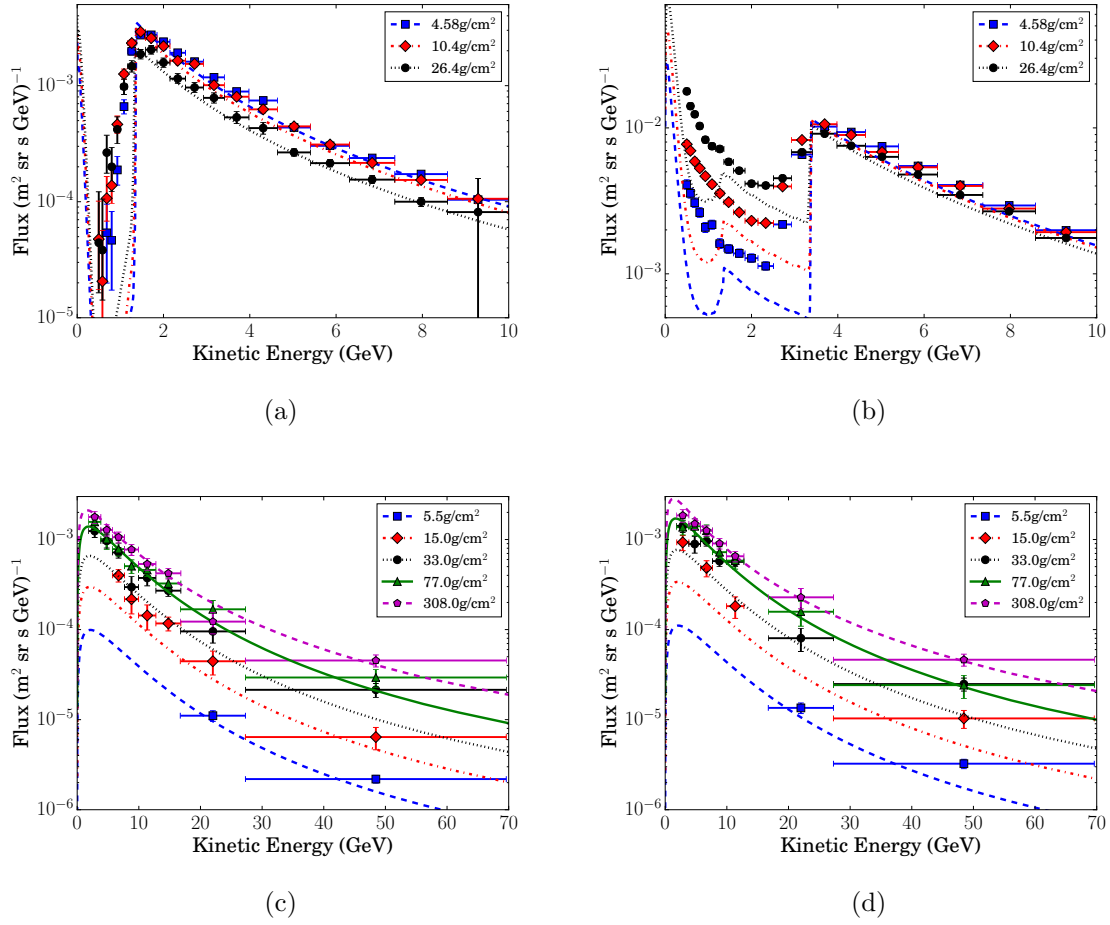Figure 1: Graphical representation of a typical measurement for GCR differential flux.

Figure 2: Measured flux data (symbols) and corresponding predicted fluxes (lines) with HZETRN at different atmospheric depths for select representative cases: (a) alphas from the BESS01 experiment, (b) protons from the BESS01 experiment, (c) negative muons from the CAPRICE98 experiment, and (d) positive muons from the CAPRICE98 experiment.
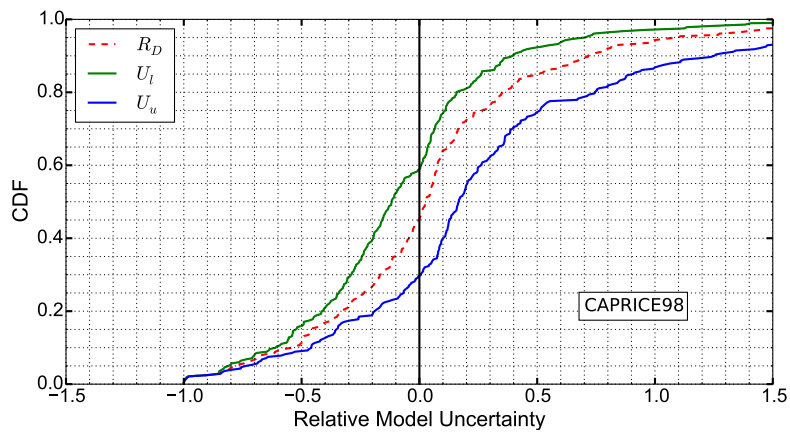
24
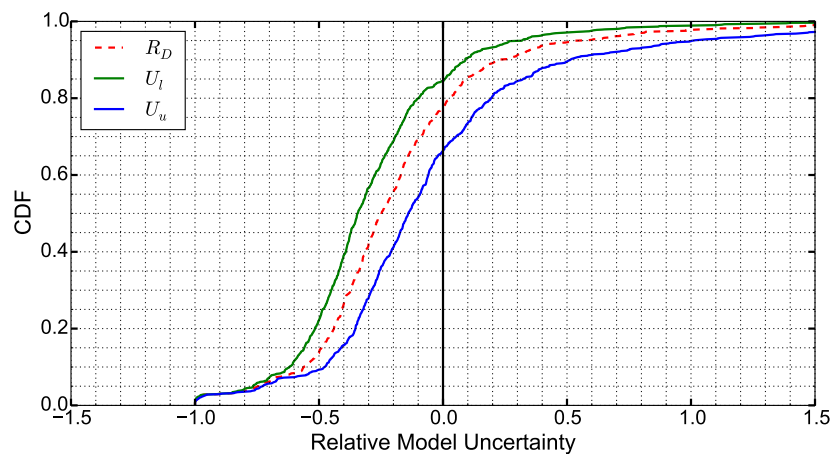
Figure 3: Cumulative distribution of HZETRN model uncertainties across all balloon-based experiments and particle types.
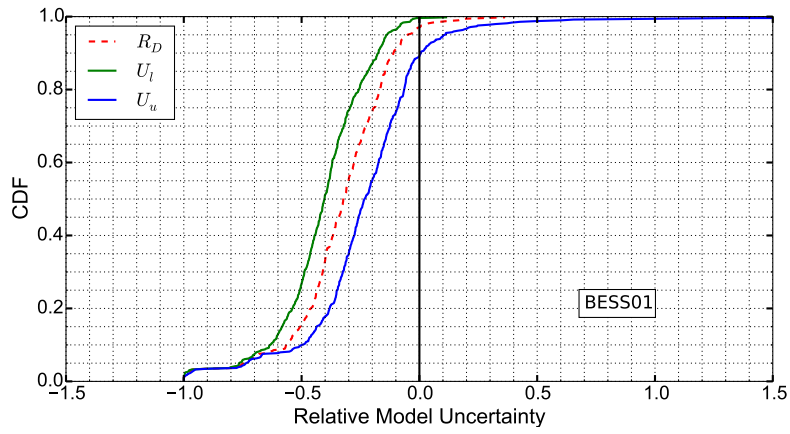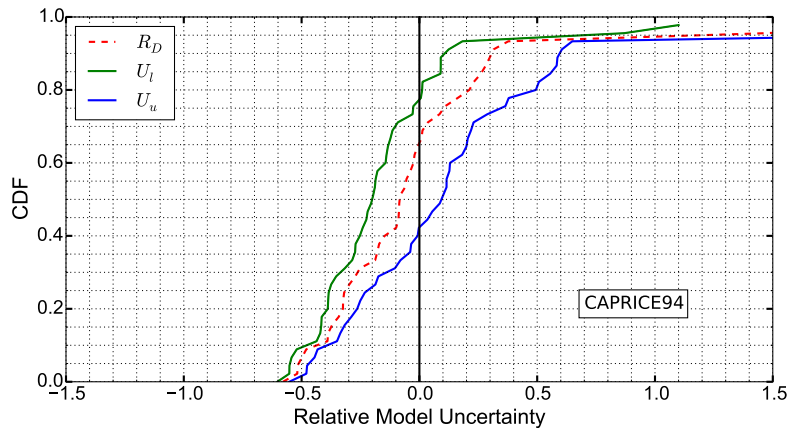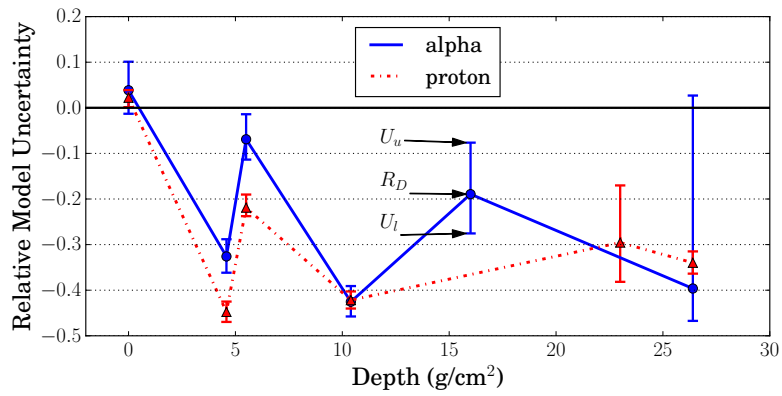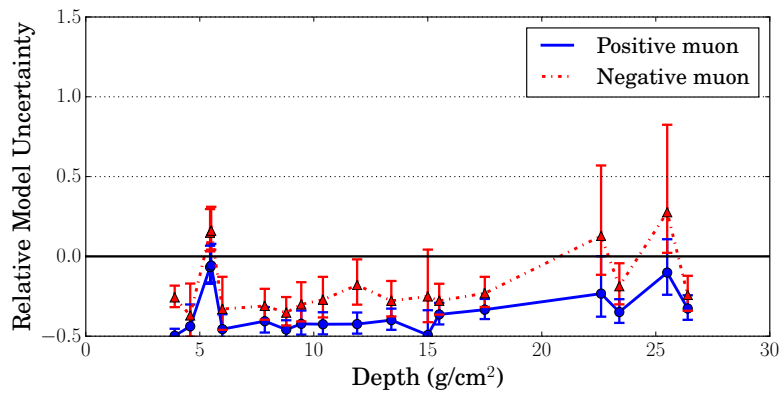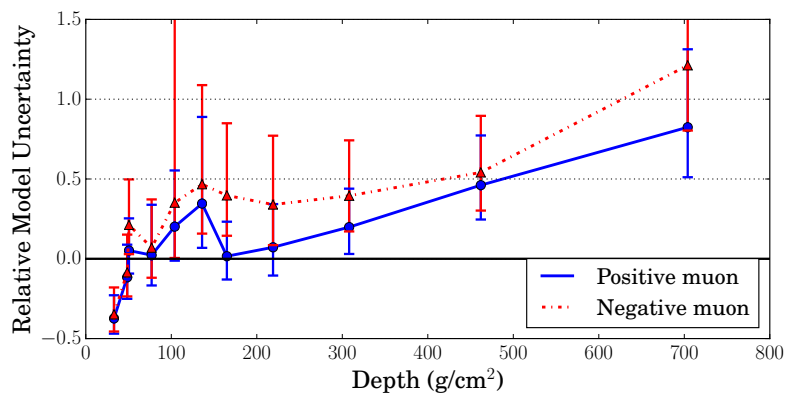
Figure 4: Cumulative distribution of HZETRN model uncertainties separated by experiment: a) BESS01, b) CAPRICE94, and c) CAPRICE98.

(a)

(b)

(c)

Figure 5: Average relative model uncertainties versus depth for a) alpha particles and protons at all measurement depths, b) muons at depths between 0 g/cm^2 and 30 g/cm^2, and c) muons at depths greater than 30 g/cm^2 .